Journal of Hazardous Materials 217–218 (2012) 100–106

Contents lists available at SciVerse ScienceDirect

Journal of Hazardous Materials

journal homepage: www.elsevier.com/locate/jhazmat

Synthesis and photocatalytic application of oriented hierarchical ZnO flower-rod architectures

Zhizhong Han[a,b,c], Lan Liao[a,b,c], Yueting Wu[c,d], Haibo Pan[a,b,c,d,**], Shuifa Shen[a,b,c], Jianzhong Chen[c,*]

[a] Fujian Engineering Research Center of Functional Materials, Yishan Campus, Fuzhou University, Fuzhou, Fujian 350002, China
[b] Institute of Research on the Functional Materials, Yishan Campus, Fuzhou University, Fuzhou, Fujian 350002, China
[c] College of Chemistry and Chemical Engineering, Qishan Campus, Fuzhou University, Fuzhou, Fujian 350108, China
[d] Fujian Key Lab of Medical Instrument and Pharmaceutical Technology, Yishan Campus, Fuzhou, Fujian 350002, China

ARTICLE INFO

Article history:
Received 24 September 2011
Received in revised form 28 February 2012
Accepted 29 February 2012
Available online 8 March 2012

Keywords:
ZnO flower-rod arrays
Photocatalytic device
Photoelectrochemical properties
Photodegradation
Rhodamine B

ABSTRACT

An oriented hierarchical ZnO flower-rod arrays (FRs) were prepared on indium doped tin oxide (ITO) glass using a facile solution-based method assisted with ZnO seed layer. And the as-prepared ZnO FRs/ITO was used as a convenient photocatalytic device that recycled without centrifugation. The results show that ZnO FRs are wurtzite phase with single crystalline grown along the [0 0 1] direction. The photoluminescence (PL) spectra illustrate that there are more oxygen vacancies on the surface of ZnO FRs compared with ZnO nanoparticles (NPs). The electrochemical methods using Rhodamine B (RhB) as electrolyte are also performed to study on the photodegradation mechanism where RhB is acted as photocatalytic substrate. For ZnO FRs, the higher photoinduced currents under UV irradiation and current density prove that the recombination of electron–hole pairs is restrained with oxygen vacancies, and the lower charge transfer resistance suggest that the charges could move quickly through ZnO oriented structures. Therefore, the photocatalytic activity is enhanced by ZnO FRs compared with ZnO NPs, and RhB degradation efficiency of ZnO FRs photocatalysts is nearly 100% by UV irradiation for 1.5 h.

1. Introduction

Since environmental problems such as air and water pollution have become a block for economic development and human health, semiconductor based photocatalytic reactions have attracted intense interest as an effective candidate for purifying contaminants [1,2]. Among the various semiconductors, ZnO is a nontoxic inorganic semiconductor which could provide such potentially useful features as high mobility, excellent chemical and thermal stability, high transparency and biocompatibility [3,4]. Additionally, ZnO is a wide-direct gap semiconductor with a high exciton binding energy of 60 meV and bandgap energy of 3.37 eV at room temperature [5], and its photodegradation mechanism has been proven to be similar to that of TiO_2 [6]. Therefore, ZnO can be regarded as a promising photocatalytic material in the ultraviolet spectral range, and be widely applied in recent years [7–10]. Beside its applications in photocatalysis, ZnO has been extensively studied for use in various functional devices, including gas sensors [11–13], transistors [3], piezoelectric transductions [14], solar cells [15–17], photosensors [5], light-emitting diodes [18] and so on.

The properties of ZnO are impacted by the microstructures of the materials, such as crystal size, orientation and morphology, aspect ratio and even crystalline density [19]. The surface and style of crystal stacked also have a crucial role in many application, including photocatalysts, transducers, varistors, and sensors. ZnO probably has the largest family of nanostructures among materials exhibiting abundant nanostructure configurations, for instance, nanowires [20,21], nanorods [22], nanotubes [23], hollow nanospheres [24,25], nanobelts [26], disk-like nanostructures [27], and 3D ZnO superstructures [28]. Oriented nanostructures, such as arrays of nanorod, shorten the electron transport pathways and promote the accessibility of the nanostructured electrode to hole-transporting materials [29], and the direct electrical pathways ensure the rapid collection of carriers generated [17]. Thus, the controlled synthesis of ZnO nanoarrays on a large scale represents very attractive scientific and technological problems to be solved. And also, the properties and activities of crystalline materials depend on their exposed crystal faces. ZnO (0 0 1) planes have been found to be chemically active whereas $(0\,0\,\bar{1})$ planes are inert [30,31]. It is illustrated that the exposed crystal faces of oriented ZnO rods and flowers are mainly composed of (0 0 1) planes [32,33]. In addition, one factor of depressing the photodegradation efficiency is

* Corresponding author.
** Corresponding author at: College of Chemistry and Chemical Engineering, Qishan Campus, Fuzhou University, Fuzhou, Fujian 350108, China.
Tel.: +86 591 22866127; fax: +86 591 22866127.
E-mail addresses: hbpan@fzu.edu.cn (H. Pan), j.z.chen@fzu.edu.cn (J. Chen).

0304-3894/$ – see front matter © 2012 Elsevier B.V. All rights reserved.
doi:10.1016/j.jhazmat.2012.02.074

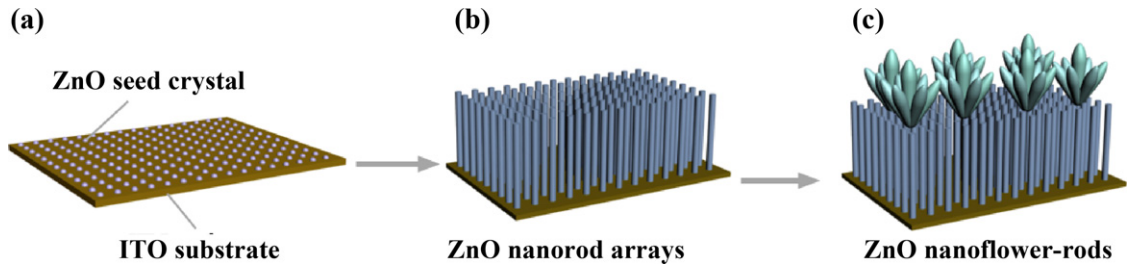

Fig. 1. Schematic process for fabricating vertically aligned ZnO flower-rod arrays on ITO substrate.

that the photocatalysts in the form of particulates are needed to filtrate and/or centrifugate after treatment of pollutants [34]. Once the photocatalysts are integrated with ITO, the filtration and/or centrifugation is not demanded but readily withdrawing the association from the solution. Therefore, it should be valuable to engage in the work on preparing oriented ZnO rods and flowers based on ITO and applying for photocatalysts.

The oriented hierarchical ZnO 1D–3D (nanorod-flower) structures have a higher areal proportion of exposed (0 0 1) faces, which are active crystal faces, and may enhance the photocatalytic activity. To authors' best knowledge, although ZnO oriented structures have been extensively studied in many respects as described above, there is still no report about the hierarchical architectures based on ITO. In the work, the ZnO nanoflower-rod arrays (ZnO FRs) are prepared through a simple solution-based method assisted with ZnO seed layer. The process is schematically shown in Fig. 1. It is modeled as three steps in aqueous solution: (i) seeding of the substrate with ZnO nanocrystals (Fig. 1a), (ii) growth of ZnO nanorod arrays on ITO substrates from ZnO seeds (Fig. 1b), (iii) building of ZnO nanoflowers onto the nanorod arrays as a result of aggregated ZnO nuclei in nucleation process (Fig. 1c). The as-prepared ZnO FRs/ITO is used as a photocatalytic device, which is convenient to recycle without centrifugation. The photogenerated currents density, photoinduced behavior, and charge transfer are also investigated using electrochemical methods. The results disclose surface and interface structures of the prepared samples, and then the photodegradation mechanism is induced in detail.

2. Experimental

2.1. Preparation of hierarchical ZnO FRs architectures based on ITO

Oriented ZnO FRs were grown on ITO substrates (HeptaChroma Solar Tech., 15 Ω/sq). Before the ZnO FRs growth, the substrates were cleaned by sonication in detergent, acetone, ethanol, and deionized water, and then dried in an oven. The substrates were then seeded by spin coating (1000 rpm, 50 s) with 6 mM zinc acetate dihydrate ($Zn(Ac)_2{\cdot}2H_2O$, 99%, Sino Chem. Reagent, 5 mM) in ethanol, followed by thermal decomposition at 300 °C for 20 min. The seeded substrates were placed in an aqueous solution containing 39 mM zinc nitrate hexahydrate ($Zn(NO_3)_2{\cdot}6H_2O$, 99%, Sino Chem. Reagent, 25 mM), 12.5 mM hexamethylenetetramine (HMTA, 99%, Sino Chem. Reagent), 5 mM polyethylenimine (PEI, 99%, Aladdin Reagent), and 0.35 M ammonium hydroxide ($NH_3{\cdot}H_2O$, 25–28%, Sino Chem. Reagent) at 83 °C for 1–2 h, then at 90 °C for 1–2 h. Finally, the ZnO samples were calcined in air at 450 °C for 30 min to enhance crystallinity.

2.2. Characterization and photocatalytic measurements

For necessarily characterizing, ZnO FRs were scraped off from the ITO with a blade. Crystalline structures of ZnO FRS were analyzed by powder X-ray diffraction (XRD, X'pert, Philips, Holland). Surface morphologies of the samples across the entire substrate were characterized by field-emission scanning electron microscopy (FE-SEM, Nova NanoSEM 230, FEI, USA), while the transmission electron microscope (TEM, Tecnai G2 F20 S-TWIN, 200 kV, FEI, USA) was used to examine the morphology of single rod or flower. The UV–vis diffuse reflectance spectra (DRS) were measured on a Perkin-Elmer Lambda 900 spectrophotometer. The photoluminescence (PL) spectra were recorded at room temperature employing a Cary Eclipase (Varian, USA). For measuring DRS and PL, ZnO FRs were removed from the ITO. And in PL measurement, ZnO FRs and ZnO NPs were dispersed in water. The electric properties of the samples were performed with an electrochemical workstation (CHI 660D, CH Instrument Company, China). All electrochemical analyses were executed using a conventional three-electrode system. The working electrode was an as-prepared ZnO FRs/ITO or ZnO NPs (Alfa Aesar, power)/ITO created through spin coating. A platinum wire and a saturated Ag/AgCl electrode were used as a counter and a reference electrode, respectively. The electrolyte solution was 0.1 M Na_2SO_4 solution and Rhodamine B (RhB) aqueous solution with a concentration of 50 μM. The Na_2SO_4 solution was used as the supporting electrolyte.

For photocatalytic measurement, the device of ZnO-FRs/ITO (2 cm × 2 cm) was immersed into 50 mL RhB aqueous solution (50 μM), and was subsequently irradiated using a UV lamp (36 W, Philip PL-L). Then at a definite time interval, 4 mL samples were withdrawn for analysis using a UV–vis spectrophotometer (PE Lambda 900). The degradation efficiency was defined as $\eta = (1 - C/C_0) \times 100\%$, where C and C_0 were the equilibrium concentration of RhB after and before UV irradiation. And the concentration of RhB was linear proportion to absorption (A), thus $C/C_0 = A/A_0$.

3. Results and discussion

3.1. Structures analysis of ZnO FRs

In this work, the HMTA and ammonium hydroxide were used to form the hydroxide ions, which reacted with Zn^{2+} to form ZnO. The chemical reactions for the formation of the ZnO precursor can be described as follows [4,35]

$$(CH_2)_6N_4 + 6H_2O \leftrightarrow 6HCHO + 4NH_3 \quad (1)$$

$$NH_3 + H_2O \leftrightarrow NH_4^+ + OH^- \quad (2)$$

$$Zn^{2+} + 4NH_3 \leftrightarrow Zn(NH_3)_4^{2+} \quad (3)$$

$$Zn^{2+} + 2OH^- \rightarrow Zn(OH)_2 \quad \text{or} \quad Zn(NH_3)_4^{2+} + 2OH^- \rightarrow Zn(OH)_2(NH_3)_4 \quad (4)$$

$$Zn(OH)_2 \rightarrow ZnO + H_2O \quad \text{or} \quad Zn(OH)_2(NH_3)_4 \rightarrow ZnO + H_2O + 4NH_3 \quad (5)$$

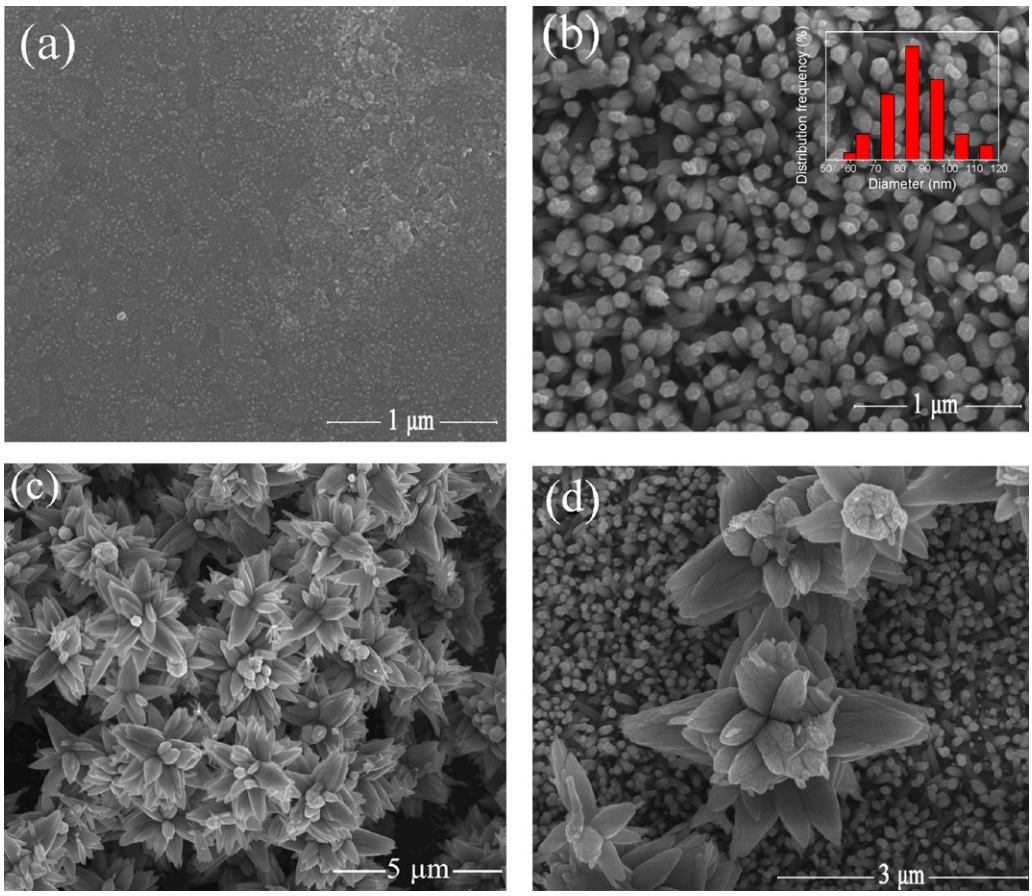

Fig. 2. The FE-SEM images for seeded ITO substrate (a), ZnO rod arrays (b) and (c, d) ZnO FRs.

Morphological analyses of ZnO FRs are illustrated in Fig. 2, and all the samples were not removed from ITO but still on the ITO. The image of seeded substrate surface (Fig. 2a) shows that the seeds are distributed uniformly and compactly. The ZnO nanorod array is displayed with a rod density of about 2.3×10^9 rods/cm^2 in Fig. 2b. As shown in the insert of Fig. 2b, most of the rod diameters are between 70 nm and 100 nm, and the average diameter is 88 nm. Further, ZnO nanoflowers are spreaded onto the nanorod arrays (Fig. 2c and d). In Fig. 2c, there are many flowers, but the rods are not obvious, because the flowers are larger and cover rod arrays. However, the flowers and rods can be exhibited simultaneously in Fig. 2d. The XRD pattern of ZnO FRs is shown in Fig. 3. Three distinct peaks at 31.8°, 34.4°, and 36.3° are observed, which are representing (1 0 0), (0 0 2), and (1 0 1) ZnO crystal planes. It is assigned to pure wurtzite ZnO phase denoting $P6_3mc$ space group as cross-referenced to JCPDS 36-1451 card. And the lattice constants are calculated as $a = 0.3250$ nm and $c = 0.5207$ nm. It has been found that the peak of ZnO nanorods which is located at 34.4° and indexed to (0 0 2) crystal plane is enhanced [36]. However, the peak at 34.4° is not enhanced in our work. Since flowers are more and larger than rods, the intensity of peak is not decided by rods but flowers.

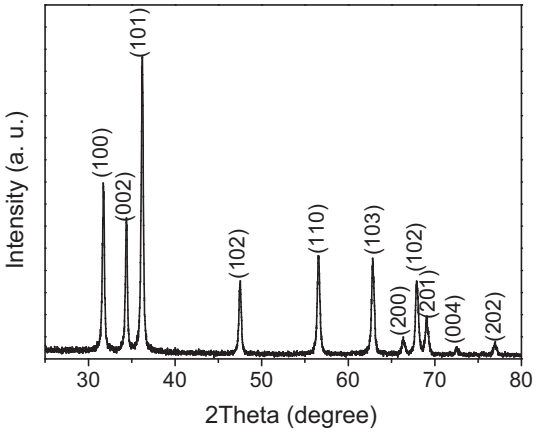

Fig. 3. XRD pattern of ZnO FRs.

In order to obtain detailed information about the microstructure of ZnO FRs, TEM observations are carried out (Fig. 4). From Fig. 4a and b, they show that the petals of ZnO nanoflowers are cone-like, with a length about 1.2–1.5 μm. The selected area electron diffraction (SAED) pattern (inset in Fig. 4a) confirms that the flower crystal is single crystalline and the direction of the growth axis is [0 0 1]. Fig. 4c and d displays the microstructure of rods that each rod is about 0.9–1.1 μm long. The high resolution TEM (HR-TEM) image from lower inset in Fig. 4d shows the lattice spacing is around 0.26 nm, which corresponds to the interspacing of the (0 0 2) planes, indicating the [0 0 1] direction (c axis) being the preferential growth direction of ZnO nanorods. The fast Fourier transform (FFT) pattern (upper inset in Fig. 4d) also confirms the estimation.

The thermodynamically stable crystallographic phase of ZnO is wurtzite, which is a hexagonal crystal system. In the hexagonal close packed lattice, Zn atoms occupy half of the tetrahedral sites, and the octahedral sites are empty. Hence, there are plenty of sites for ZnO to accommodate intrinsic (namely Zn interstitials) defects and extrinsic dopants. The typical crystal habits of wurtzite ZnO exhibit a basal polar plane (0 0 $\bar{1}$), a nonpolar ($\bar{1}$ 0 0) face (and C_{6v} symmetric ones) and a tetrahedron corner-exposed polar (0 0 1) face vertical to the c axis. The "low-symmetry" nonpolar faces with

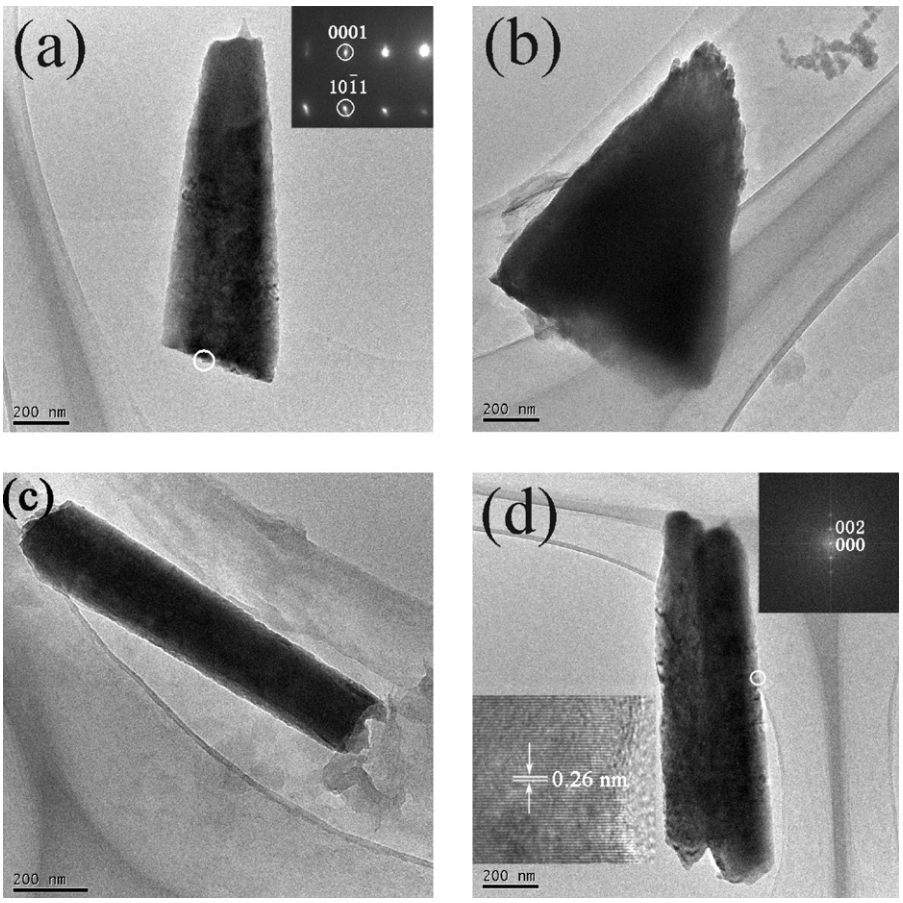

Fig. 4. TEM image of ZnO FRs: a petal of the flowers, the inset is the corresponding SAED pattern (a); another petal of the flowers (b); a separate rod (c); separated rods, the lower inset is high-resolution TEM image, the upper inset is FFT pattern (d).

3-fold coordinated atoms are the most stable ones. Additionally, there is no center of inversion in the wurtzite crystal structure, and so an inherent asymmetry along the *c* axis is present allowing the anisotropic growth of crystal along the [0 0 1] direction. Therefore, the hexagon elongated along the *c* axis should be the theoretical and most stable crystal habit [37]. But Tian et al. suggest that the ZnO crystals are mostly randomly oriented at the beginning [19]. Thereby, in the present work, the asymmetry structural characteristic is used to design oriented ZnO nanorod arrays on a seeded layer, which offer an initial direction for the growth.

Synthesizing ZnO flower superstructures usually requires the formation of aggregated ZnO nuclei in an initial homogeneous nucleation process [32]. In this process, a large number of ZnO growth units lead to a burst in homogeneous nucleation forming aggregated ZnO nuclei. The ZnO crystals produced during the initial growth stage have crystalline grains and boundaries, which contain more defects than other regions and are not thermodynamically stable. Each grain of the initial ZnO crystals could grow primarily along one growth direction, and secondary growth from the defects may also have occurred due to the large number of growth units. The crystal surfaces containing defects tend to further decrease their energy through surface reconstruction, which provides active sites for secondary nucleation. Accordingly, complex ZnO flower structures form in the presence of abundant growth units.

3.2. Optical properties for ZnO FRs and ZnO NPs

The UV–vis diffuse reflectance spectra of the as-prepared ZnO FRs are shown in Fig. 5a, which are compared to ZnO nanoparticles (NPs). The ZnO FRs exhibit stronger absorption than ZnO NPs in UV region, and its adsorption edge at about 385 nm is bathochromic shift of 6 nm. Thus, ZnO FRs can assimilate more luminous energy and enhance photocatalytic activities.

Room-temperature PL spectra induced by 325 nm excitation wavelength were collected in the range from 350 to 600 nm in Fig. 5b for ZnO FRs and NPs, respectively. The spectra are characteristics of ZnO nanostructures with different contributions of near band gap emission at ~380 nm and visible emission (>400 nm). Compared with ZnO NPs, the intensity of the UV emission for ZnO FRs decreases, contrarily, the visible emission increases. The UV emission is related to the near band-edge emission of ZnO. The emission originates in the recombination of free excitons through an exciton–exciton collision process [38]. On the other hand, the visible spectral emission (>400 nm) is attributed to deep defect levels located in the gap [39]. In Fig. 5b, two emission peaks centered at about 446 and 520 nm are observed, which correspond to shallow donor-oxygen vacancies and oxygen vacancies, respectively [40]. The two defects work as electron donors and can trap the photogenerated electrons temporarily to reduce the surface recombination of electrons and holes. The dramatic differences in the PL emission spectra between ZnO FRs and NPs illustrate that more defects exist in the former that could hamper the recombination of photogenerated electrons with holes.

3.3. Photoelectrochemical response of ZnO FRs and ZnO NPs based on ITO

In order to confirm the photocatalytic mechanism and the effect of oxygen vacancies for ZnO FRs and ZnO NPs, the electrochemical methods were carried out under UV irradiation. The

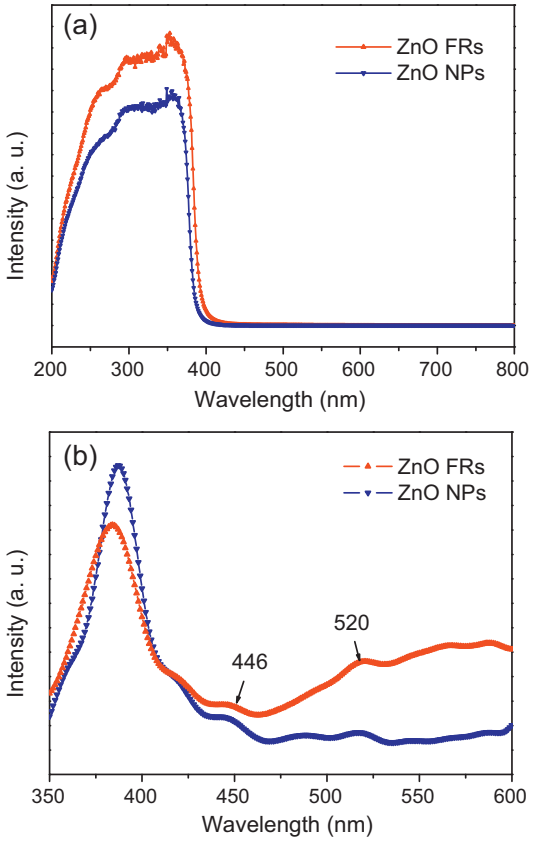

Fig. 5. UV–vis diffuse reflectance spectra (a) and PL spectra of ZnO FRs and ZnO NPs (b).

photoelectrochemical process can simulate the action of photoexcited current for ZnO FRs and ZnO NPs as photocatalysts, and also, the electrolyte used in photoelectrochemical process is RhB, just as photocatalytic substrate as shown later. Fig. 6a depicts cyclic voltammograms (*C*–*V*) curves with different working electrodes. The potential was scanned from −0.6 V to 1.2 V, then contrarily, from 1.2 V and ended at −0.6 V. The scan rate was 100 mV s^{-1}. In this progress, the pH is reduced. And according to the results of *C*–*V* measure, the cell reactions could be depicted as:

$$(\text{anode})\text{RhB} + m\text{H}_2\text{O} - ne^- \rightarrow \text{oxidationproducts} + n\text{H}^+ \quad (6)$$

$$(\text{cathode})n\text{H}^+ + ne^- \rightarrow n/2\text{H}_2 \quad (7)$$

It can be acquired from Fig. 6a that the current density of ZnO FRs is higher than that of ZnO NPs in oxidative decomposition of RhB (Eq. (6)). Space charge region on ZnO FRs is developed along crystal growth direction, thus photogenerated electrons flow to the bulk ZnO through space charge region easily according to the current density of ZnO FRs [41]. It could induce decreasing the recombination of photoinduced electrons and holes as revealing higher electron transfer rate from RhB molecules. The result also indicates that the photodegradation of RhB as described later is an oxidation reaction. At the same time, there is not any significant peak for bare ITO, indicating that bare ITO has less photoelectrochemical activity for photocatalytic decomposition of RhB. So it assumes that ZnO FRs have better photocatalytic performance.

To further investigate the photoinduced behaviors and photoelectrochemical properties, the amperometric *I*–*t* curves was measured upon the on-off illumination with UV light (Fig. 6b), and the applied voltage was 0.85 V. When the UV light is turned on, the electrons in the valence band can be excited to the conduction band and photocurrent is formed. The photocurrent is balanced

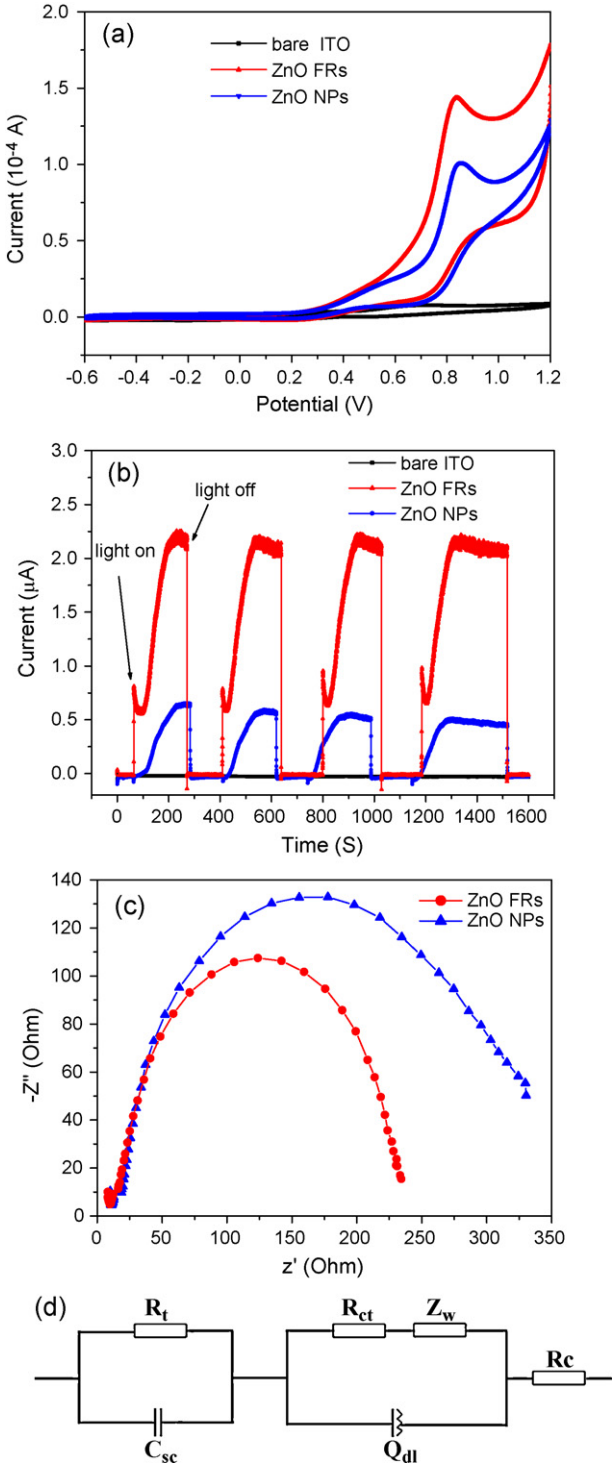

Fig. 6. The electrochemical properties of bare ITO, ZnO FRs, and ZnO NPs: cyclic voltammograms (a), amperometric *I*–*t* curves (b), electrochemical impedance spectroscopy (c), and schematic model of equivalent circuit (d).

as the recombination of electrons and holes is saturated. And the photocurrent is disappeared once the light is turned off. When the light is subsequently switched on and off, a series of almost identical signal are obtained. Fig. 6b portrays that the photoinduced current of ZnO FRs is strongest compared with bared ITO and ZnO NPs electrodes. The trend agrees on the results obtained by cyclic voltammetry, and illuminates that more photoinduced carriers exist in degradation process, that is, recombination of e_{cb}^- and h_{vb}^+ is hindered. It is also found from Fig. 6b that the transient

Table 1
Parameters extracted from fitted results of EIS spectra for each sample using RhB as electrolyte.

	R_t (Ω)	C_{sc} (μF)	R_{ct} (Ω)	Z_w (Ssec$^{0.5}$)	Q_{dl} (Ssec^n)	R_c (Ω)
Zn FRs	9.076	12.52	211.6	0.03208	2.621×10^{-5}	8.369
Zn NPs	13.93	12.48	268.9	0.05977	3.001×10^{-5}	9.008

photocurrent shows a slow response when the light is switched on. The photoinduced electrons trapped in the surface defects (e.g. oxygen vacancies) of ZnO nanostructures are responsible for the slow photocurrent response, since only a part of the photoinduced electrons can transport to ITO until the surface defects are filled [42]. Thus, this suggests that ZnO FRs contain more surface defects, which are beneficial in separating photoinduced electrons and holes. In addition, the photocatalysts (ZnO FRs and NPs) put up a reproducible property.

Electrochemical impedance spectroscopy (EIS) is used to measure the current response to the application of an ac voltage as a function of the frequency and characterizing electrochemical interfacial reactions [41,43]. Fig. 6c is electrochemical impedance spectroscopy for ZnO FRs and ZnO NPs. EIS experiments were carried out in the frequency from 0.001 to 100 kHz at dc bias of 0.7 V. The magnitude of the alternative signal was 10 mV. Equivalent circuit comprises serial combination of bulk electrolyte resistance (Rc), interfacial reaction impedance between ZnO and electrolyte, and electron transfer at the interface between ZnO nanostructures and ITO (Fig. 6d). Interfacial reaction impedance includes charge transfer resistance (R_{ct}) that is in series connected with a diffusion element Z_w, and the two being in parallel with a electrochemical double-layer capacitive (constant phase angle) element Q_{dl}. The impedance between ZnO nanostructures and ITO consists of space charge capacitance (C_{sc}), and the resistance of ZnO/ITO contact (R_t). Table 1 shows that ZnO FRs have a lower charge transfer resistance than nanoparticles. The oxygen vacancies on ZnO FRs surface lead to decrease the probability of exciton–exciton recombination as exhibiting higher electron transfer rate from RhB molecules. At the same, the connection between ZnO FRs and ITO is compact because ZnO FRs have grown directly on the substrate. And the oriented ZnO FRs apply a pathway for charge quickly transferring among ZnO nanostructures, then R_t is decreased. So ZnO FRs show a lower charge transfer resistance and are envisaged as a higher photocatalytic activity.

3.4. Photocatalytic activities and mechanism

The photocatalytic activity of the as-prepared ZnO FRs and ZnO NPs on the RhB degradation was investigated in the presence of UV light radiation. Fig. 7 shows the degradation rates of RhB without catalysts and using ZnO nanostructures. After irradiation for 3 h, the degradation efficiency (η) of RhB is found to be about 27.4% (self-degradation) and 83.7% (with ZnO NPs), respectively. While for a shorter irradiating time, η by using ZnO FRs lead to nearly 100% degradation of the identical RhB solutions during 1.5 h. Obviously, the as-prepared ZnO FRs can work as effective photocatalysts.

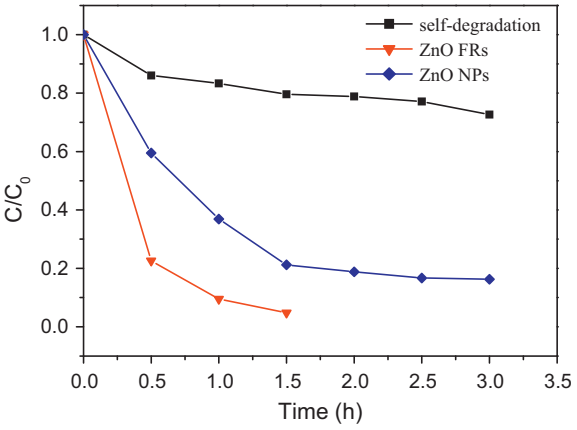

Fig. 7. Degradation rate of Rhodamine B without photocatalyst and with ZnO FRs and ZnO NPs, respectively.

The corresponding photocatalytic reaction process can be formulated as [34,44]:

$$ZnO + h\nu \rightarrow e_{cb}^- + h_{vb}^+ \quad (8)$$

$$e_{cb}^- + O_2 \rightarrow O_2\bullet^- \quad (9)$$

$$h_{vb}^+ + OH^- \rightarrow \cdot OH \quad (10)$$

$$RhB + \cdot OH \rightarrow \text{oxidationproducts} \quad (11)$$

$$h_{vb}^+ + RhB \rightarrow \text{oxidationproducts} \quad (12)$$

In general, when semiconductor nanocrystals are irradiated by light with energy higher or equal to the band gap, an electron (e_{cb}^-) in the valence band (VB) can be excited to the conduction band (CB) with the simultaneous generation of a hole (h_{vb}^+) in the VB. Excited state e_{cb}^- and h_{vb}^+ can recombine and get trapped in metastable surface states, or react with electron donors and electron acceptors adsorbed on the semiconductor surface. In other words, the photoelectron is easily trapped by electron acceptors like adsorbed O_2, whereas the photoinduced holes can be easily trapped by electronic donors, such as OH^- or organic pollutants, to further oxidize organic dye [44]. At the same time, the photocatalytic activity does not only depend on the surface adsorption ability, but also relates to the type and concentration of oxygen defects on the surface and/or surface layers [45]. Since the oxygen vacancies can serve as the electron capturing center to restrain the recombination of e_{cb}^- and h_{vb}^+ as described above. In addition, the oxygen vacancies could work in generating active species on the surfaces of semiconductor material, therefore, are beneficial to the photodegradation of organic dye [38]. On the specific surface of ZnO FRs, more oxygen vacancies occur and capture the photoinduced electrons, the oriented arrays provide a pathway for charge quickly transferring, and the oriented hierarchical ZnO FRs structures have a higher areal proportion of exposed (0 0 1) active faces. Thereby, the device of ZnO FRs/ITO represents predominant photodegradation efficiency.

4. Conclusions

In summary, we have demonstrated the first fabricated of oriented hierarchical ZnO flower-rod architectures based on ITO and the association of ZnO FRs/ITO as a convenient and efficient photocatalytic device. The XRD pattern elucidates the as-prepared ZnO FRs are pure wurtzite phase. While the length of flower petal and rod is 1.2–1.5 and 0.9–1.1 μm, respectively. The HR-TEM and SAED image indicate that ZnO FRs are single crystal grown along the *c*-axis, and the flowers are cone-like building blocks. Additionally, these structures expose more active crystal faces. ZnO FRs show higher photocatalytic activity compared with ZnO NPs. Through PL spectra, it is found that ZnO FRs have more surface oxygen vacancies, which could restrain the recombination of photoinduced electron–hole pairs. Further, the mechanism is validated with electrochemical methods, including *C–V* curves, *I–t* curves, and EIS. The results confirm that the photoelectrochemical characteristics

are enhanced by ZnO FRs, and then the photocatalytic ability is improved. Finally, we expect that this structure could be found in applications in solar cells, sensors and other devices.

Acknowledgements

The authors gratefully acknowledge the financial support from National Natural Science Foundation of China (91022025, 51072036, and J0830414), Fujian Natural Science Foundation (2008J0330), and Fujian Department of Science and Technology (2008F5033 and 2009I0016).

References

[1] M.R. Hoffmann, S.T. Martin, W. Choi, D.W. Bahnemann, Environmental applications of semiconductor photocatalysis, Chem. Rev. 95 (1995) 69–96.
[2] C.L. Ren, B.F. Yang, M. Wu, J. Xu, Z.P. Fu, Y. Lv, T. Guo, Y.X. Zhao, C.Q. Zhu, Synthesis of Ag/ZnO nanorods array with enhanced photocatalytic performance, J. Hazard. Mater. 182 (2010) 123–129.
[3] B.S. Ong, C.S. Li, Y.N. Li, Y.L. Wu, R. Loutfy, Stable, solution-processed, high-mobility ZnO thin-film transistors, J. Am. Chem. Soc. 129 (2007) 2750–2751.
[4] L. Schmidt-Mende, J.L. MacManus-Driscoll, ZnO – nanostructures, defects, and devices, Mater. Today 10 (2007) 40–48.
[5] Y.K. Su, S.M. Peng, L.W. Ji, C.Z. Wu, W.B. Cheng, C.H. Liu, Ultraviolet ZnO nanorod photosensors, Langmuir 26 (2010) 603–606.
[6] J.T. Tian, L.J. Chen, Y.S. Yin, X. Wang, J.H. Dai, Z.B. Zhu, X.Y. Liu, P.W. Wu, Photocatalyst of TiO_2/ZnO nano composite film: preparation, characterization, and photodegradation activity of methyl orange, Surf. Coat. Tech. 204 (2009) 205–214.
[7] O. Akhavan, Graphene nanomesh by ZnO nanorod photocatalysts, ACS Nano. 4 (2010) 4174–4180.
[8] N. Kislov, J. Lahiri, H. Verma, D.Y. Goswami, E. Stefanakos, M. Batzill, Photocatalytic degradation of methyl orange over single crystalline ZnO: orientation dependence of photoactivity and photostability of ZnO, Langmuir 25 (2009) 3310–3315.
[9] X.Y. Yang, A. Wolcott, G.M. Wang, A. Sobo, R.C. Fitzmorris, F. Qian, J.Z. Zhang, Y. Li, Nitrogen-doped ZnO nanowire arrays for photoelectrochemical water splitting, Nano Lett. 9 (2009) 2331–2336.
[10] P. Li, Z. Wei, T. Wu, Q. Peng, Y.D. Li, Au–ZnO hybrid nanopyramids and their photocatalytic properties, J. Am. Chem. Soc. 133 (2011) 5660–5663.
[11] M.J.S. Spencer, I. Yarovsky, ZnO nanostructures for gas sensing: Interaction of NO_2, NO, O, and N with the ZnO $(1\,0\,\bar{1}\,0)$ surface, J. Phys. Chem. C 114 (2010) 10881–10893.
[12] N.F. Hamedani, A.R. Mahjoub, A.A. Khodadadi, Y. Mortazavi, Microwave assisted fast synthesis of various ZnO morphologies for selective detection of CO, CH_4 and ethanol, Sens. Actuators B 156 (2011) 737–742.
[13] S.L. Bai, X. Liu, D.Q. Li, S. Chen, R.X. Luo, A.F. Chen, Synthesis of ZnO nanorods and its application in NO_2 sensors, Sens. Actuators B 153 (2011) 110–116.
[14] D. Choi, M.Y. Choi, W.M. Choi, H.J. Shin, H.K. Park, J.S. Seo, J. Park, S.M. Yoon, S.J. Chae, Y.H. Lee, S.W. Kim, J.Y. Choi, S.Y. Lee, J.M. Kim, Fully rollable transparent nanogenerators based on graphene electrodes, Adv. Mater. 22 (2010) 2187–2192.
[15] J.J. Wu, Y.R. Chen, W.P. Liao, C.T. Wu, C.Y. Chen, Construction of nanocrystalline film on nanowire array via swelling electrospun polyvinylpyrrolidone-hosted nanofibers for use in dye-sensitized solar cells, ACS Nano. 4 (2010) 5679–5684.
[16] F.P. Yan, L.H. Huang, J.S. Zheng, J. Huang, Z. Lin, F. Huang, M.D. Wei, Effect of surface etching on the efficiency of ZnO-based dye-sensitized solar cells, Langmuir 26 (2010) 7153–7156.
[17] M. Law, L.E. Greene, J.C. Johnson, R. Saykally, P.D. Yang, Nanowire dye-sensitized solar cells, Nature Mater. 4 (2005) 455–459.
[18] N. Saito, H. Haneda, T. Sekiguchi, N. Ohashi, I. Sakaguchi, K. Koumoto, Low-temperature fabrication of light-emitting zinc oxide micropatterns using self-assembled monolayers, Adv. Mater. 14 (2002) 418–421.
[19] Z.R. Tian, J.A. Voigt, J. Liu, B. Mckenzie, M.J. Mcdermott, M.A. Rodriguez, H. Konishi, H.F. Xu, Complex and oriented ZnO nanostructures, Nature Mater. 2 (2003) 821–826.
[20] Y. Sun, N.A. Fox, G.M. Fuge, M.N.R. Ashfold, Toward a single ZnO nanowire homojunction, J. Phys. Chem. C 114 (2010) 21338–21341.
[21] M.K. Kim, D.K. Yi, U. Paik, Tunable, flexible antireflection layer of ZnO nanowires embedded in PDMS, Langmuir 26 (2010) 7552–7554.
[22] Y.H. Zheng, L.R. Zheng, Y.Y. Zhan, X.Y. Lin, Q. Zheng, K.M. Wei, Ag/ZnO heterostructure nanocrystals: synthesis, characterization, and photocatalysis, Inorg. Chem. 46 (2007) 6980–6986.
[23] M.S. Samuel, J. Koshy, A. Chandran, K.C. George, Electrical charge transport and dielectric response in ZnO nanotubes, Curr. Appl. Phys. 11 (2011) 1094–1099.
[24] S.S. Lo, D. Huang, Morphological variation and Raman spectroscopy of ZnO hollow microspheres prepared by a chemical colloidal process, Langmuir 26 (2010) 6762–6766.
[25] B. Fang, C.H. Zhang, G.F. Wang, M.F. Wang, Y.L. Ji, A glucose oxidase immobilization platform for glucose biosensor using ZnO hollow nanospheres, Sens. Actuators B 155 (2011) 304–310.
[26] Y.C. Yang, G.F. Wang, X.D. Li, Water molecule-induced stiffening in ZnO naobelts, Nano Lett. 11 (2011) 2845–2848.
[27] J.X. Wang, C.M.L. Wu, W.S. Cheung, L.B. Luo, Z.B. He, G.D. Yuan, W.J. Zhang, C.S. Lee, S.T. Lee, Synthesis of hierarchical porus ZnO disklike nanostructures for improved photovoltaic properties of dye-sensitized solar cells, J. Phys. Chem. C 114 (2010) 13157–13161.
[28] X.Y. Xue, Z.H. Chen, L.L. Xing, C.H. Ma, Y.J. Chen, T.H. Wang, Enhanced optical and sensing properties of one-step synthesized Pt-ZnO nanoflowers, J. Phys. Chem. C 114 (2010) 18607–18611.
[29] C.K. Xu, P.H. Shin, L.L. Cao, J.M. Wu, D. Gao, Ordered TiO_2 nanotube arrays on transparent conductive oxide for dye-sensitized solar cells, Chem. Mater. 22 (2010) 143–148.
[30] E.S. Jang, J.H. Won, S.J. Hwang, J.H. Choy, Fine tuning of the face orientation of ZnO crystals to optimize their photocatalytic activity, Adv. Mater. 18 (2006) 3309–3312.
[31] Z.L. Wang, X.Y. Kong, J.M. Zuo, Induced growth of asymmetric nanocantilever arrays on polar surfaces, Phys. Rev. Lett. 91 (2003), 185502-1:4.
[32] S. Cho, J.W. Jang, J.S. Lee, K.H. Lee, Exposed crystal face controlled synthesis of 3D ZnO superstructures, Langmuir 26 (2010) 14255–14262.
[33] L. Vayssieres, K. Keis, S.E. Lindquist, A. Hagfeldt, Purpose-built anisotropic metal oxide material: 3D highly oriented microrod array of ZnO, J. Phys. Chem. B 105 (2001) 3350–3352.
[34] S. Horikoshi, A. Saitou, H. Hidaka, N. Serpone, Environmental remediation by an integrated microwave/UV illumination method. V. thermal and nonthermal effects of microwave radiation on the photocatalyst and on the photodegradation of rhodamine-B under UV/Vis radiation, Environ. Sci. Technol. 37 (2003) 5813–5822.
[35] T. Ichikawa, S. Shiratori, Fabrication and evaluation of ZnO nanorods by liquid-phase deposition, Inorg. Chem. 50 (2011) 999–1004.
[36] H. Wagata, N. Ohashi, T. Taniguchi, K. Katsumata, K. Okada, N. Matsushita, Control of the microstructure and crystalline orientation of ZnO films on a seed-free glass substrate by using a spin-spray method, Cryst. Growth Des. 10 (2010) 4968–4975.
[37] L. Vayssieres, K. Keis, A. Hagfeldt, S.E. Lindquist, Three-dimensional array of highly oriented crystalline ZnO microtubes, Chem. Mater. 13 (2001) 4395–4398.
[38] Y. Liu, Z.H. Kang, Z.H. Chen, I. Shafiq, J.A. Zapien, I. Bello, W.J. Zhang, S.T. Lee, Synthesis, characterization, and photocatalytic application of different ZnO nanostructures in array configurations, Cryst. Growth Des. 9 (2009) 3222–3227.
[39] L.E. Greene, M. Law, J. Goldberger, F. Kim, J.C. Johnson, Y.F. Zhang, R.J. Saykally, P.D. Yang, Low-temperature wafer-scale production of ZnO nanowire arrays, Angew. Chem. Int. Ed. 42 (2003) 3031–3034.
[40] A.B. Djurišić, A.M.C. Ng, X.Y. Chen, ZnO nanostructures for optoelectronics: material properties and device applications, Prog. Quant. Electron. 34 (2010) 191–259.
[41] H.J. Yun, H. Lee, N.D. Kim, J. Yi, Characterization of photocatalytic performance of silver deposited TiO_2 nanorods, Electrochem. Commun. 11 (2009) 363–366.
[42] J.G. Yu, G.P. Dai, B.B. Huang, Fabrication and characterization of visible-light-driven plasmonic photocatalyst Ag/AgCl/TiO_2 nanotube arrays, J. Phys. Chem. C 113 (2009) 16394–16401.
[43] Q. Wang, J.E. Moser, M. Grätzel, Electrochemical impedance spectroscopic analysis of dye-sensitized solar cells, J. Phys. Chem. B 109 (2005) 14945–14953.
[44] X.P. Lin, T. Huang, F.Q. Huang, W.D. Wang, J.L. Shi, Photocatalytic activity of a Bi-based oxychloride Bi_3O_4Cl, J. Phys. Chem. B 110 (2006) 24629–24634.
[45] Y.H. Zheng, C.Q. Chen, Y.Y. Zhan, X.Y. Lin, Q. Zheng, K.M. Wei, J.F. Zhu, Y.J. Zhu, Luminescence, photocatalytic activity of ZnO manocrystals: correlation between structure and property, Inorg. Chem. 46 (2007) 6675–6682.